Anisotropy in seafloor flange, slab, and crust samples from measurements of permeability and porosity: Implications for fluid flow and deposit evolution

Jill L. Gribbin and Wen-lu Zhu

Department of Geology, University of Maryland, College Park, Maryland 20742, USA
(jgribbin@umd.edu; wzhu@umd.edu)

Margaret K. Tivey

Department of Marine Chemistry and Geochemistry, Woods Hole Oceanographic Institution, McLean
Building 201, MS 08, Woods Hole, Massachusetts 02543, USA (mktivey@whoi.edu)

[1] Seafloor hydrothermal vents accommodate the convective transfer of fluids from subsurface environments to the oceans. In addition to black smoker chimneys, a variety of other deposit-types form. Flanges protrude from the sides of edifices as horizontal ledges, below which vent fluids pool. Slabs are hydrothermally silicified layered volcaniclastic deposits. Crusts are deposits composed of previously deposited material underlain by hot fluids. Permeability and porosity measurements were conducted on flanges from Guaymas Basin and the Main Endeavour Vent Field, slabs from the Lucky Strike Vent Field, and a crust sample from the Trans-Atlantic Geotraverse (TAG) active mound. Cores taken parallel to textural layers have high permeabilities ($\approx 10^{-12}$ m^2) and porosities (30–40%) that follow a power law relationship with exponent $\alpha \approx 1$ to 2. Cores taken perpendicular to layering have permeabilities from 10^{-16} to 10^{-12} m^2 and porosities from 20 to 45%, with $\alpha \approx 5$ to 8. The two distinct trends result from the heterogeneity of textural layers within these deposits. Microstructural observations show large variations in grain packing and pore distributions between layers, consistent with flow perpendicular to layering being more susceptible to changes in permeability that result from mineral precipitation than flow parallel to layering. These results imply that the primary flow direction in these deposits is parallel to layering, whereas flow perpendicular to layering is more restricted. Quantification of anisotropic permeability provides important constraints for determination of fluid flux from these layered deposits, and temperatures, chemistry, and availability of nutrients to organisms living in and at exteriors of deposits.

1. Introduction

[2] The interaction of hot hydrothermal fluids with seawater results in both chemical and physical processes that can change the structure of active seafloor vent deposits. Much work has been done to identify the composition, structure, and evolution of these deposits from a range of vent fields. Early studies conducted on samples from the East Pacific Rise, such as those by *Haymon* [1983] and *Goldfarb et al.* [1983], analyzed the most prominent actively venting deposits, the black smoker chimneys. The rapid, high-temperature, focused fluid emission from these chimneys is in stark contrast to numerous other deposit-types that emit more diffuse fluid flow [e.g., *Haymon and Kastner*, 1981; *Lonsdale and Becker*, 1985; *Delaney et al.*, 1992; *Tivey et al.*, 1995; *Hannington et al.*, 1995; *Langmuir et al.*, 1997]. The portions of deposits subject to diffuse flow accommodate a significant transfer of fluids between the subsurface and seafloor [e.g., *Schultz et al.*, 1992; *Veirs et al.*, 2006] yet little quantitative information is available to investigate the feedback between the fluid, the evolving deposits, and the surrounding environmental conditions [*Delaney et al.*, 1992; *Lowell et al.*, 1995].

[3] The formation and evolution of vent deposits are determined by fluid flow, interactions of different fluids (hydrothermal fluid and seawater), and evolving physical and chemical environments, and can be impacted by tectonic and magmatic events [e.g., *Haymon*, 1996; *Lilley et al.*, 2003; *Bohnenstiehl et al.*, 2004]. Changes in environmental conditions, such as temperature, flow rate, and the degree of mixing, can significantly impact how deposits evolve [e.g., *Tivey and McDuff*, 1990; *Koski et al.*, 1994; *Hannington et al.*, 1995; *Tivey*, 1995]. Conversely, evolution of deposit transport properties (e.g., porosity, permeability) affects the ability of vent deposits to transfer fluids. Using data from vent fluid and deposit samples, a few modeling studies have investigated the feedback between vent deposit evolution and fluid flow, such as how fluid flow can be affected by decreases in porosity or permeability (e.g., see review by *Lowell et al.* [1995], *Woods and Delaney* [1992], *Tivey* [1995], and *Kerr* [1997]). However, missing ingredients in current models are well-constrained data on these transport properties: permeability (k), the vent deposit's ability to transmit fluid, and porosity (ϕ), the volume fraction of void space within the deposit. Systematic characterizations of the evolution of permeability and porosity relationships

(EPPRs) of vent deposits are scarce, with the exception of data from samples recovered from the Mothra Vent Field on the Endeavour Segment of the Juan de Fuca Ridge. Data from Mothra deposits show systematic variations in EPPRs that have been correlated to observable variations in mineralogy and mineral textures [*Zhu et al.*, 2007].

[4] Because vent deposits facilitate fluid transport and host diverse biological communities [e.g., *Haymon and Kastner*, 1981; *Fisher et al.*, 2007], measurements of their flow properties are critical for improving our understanding of chemical and biological systems at hydrothermal vents. The hypothesized effects of the presence of fossil worm tubes within deposits to fluid flow and deposit evolution [e.g., *Haymon and Kastner*, 1981; *Tivey and Delaney*, 1986; *Hannington and Scott*, 1988; *Tivey et al.*, 1999; *Le Bris et al.*, 2005; *Kristall et al.*, 2006] highlight the need for data on transport properties. In this study, we report permeability and porosity measurements conducted on flange, slab, and crust samples from varying locations to establish EPPRs for each deposit type.

[5] A common feature of flange, slab, and crust deposits is horizontal mineralogical layering, in part reflecting deposit formation (e.g., mineral precipitation from pooled fluid and/or cementation of debris that has settled on the horizontal surface), and in part a result of fluids percolating laterally and upwards through interconnected pores. The prevalence of layering suggests that processes controlling evolution of these deposits may be similar [*Delaney et al.*, 1992; *Tivey et al.*, 1995; *Langmuir et al.*, 1997; *Cooper et al.*, 2000]. We here use measurements of transport properties, in concert with microstructural analyses, to provide quantitative constraints on flow distribution, and new insights into pore evolution, within these vent deposits.

2. Geologic Descriptions

[6] Flanges are the most widespread of these layered deposit types (Figures 1a and 1b), and have been identified at multiple vent sites [*Lonsdale and Becker*, 1985; *Peter and Scott*, 1988; *Lisitsyn et al.*, 1989; *Delaney et al.*, 1992; *Robigou et al.*, 1993]. A flange extends horizontally from the side of a larger vent edifice, and hydrothermal fluids pool beneath the ledge. Precipitation of minerals from the pool forms layers against the underside of the flange [*Delaney et al.*, 1992]. Buoyant fluids from the pool percolate upwards through the porous
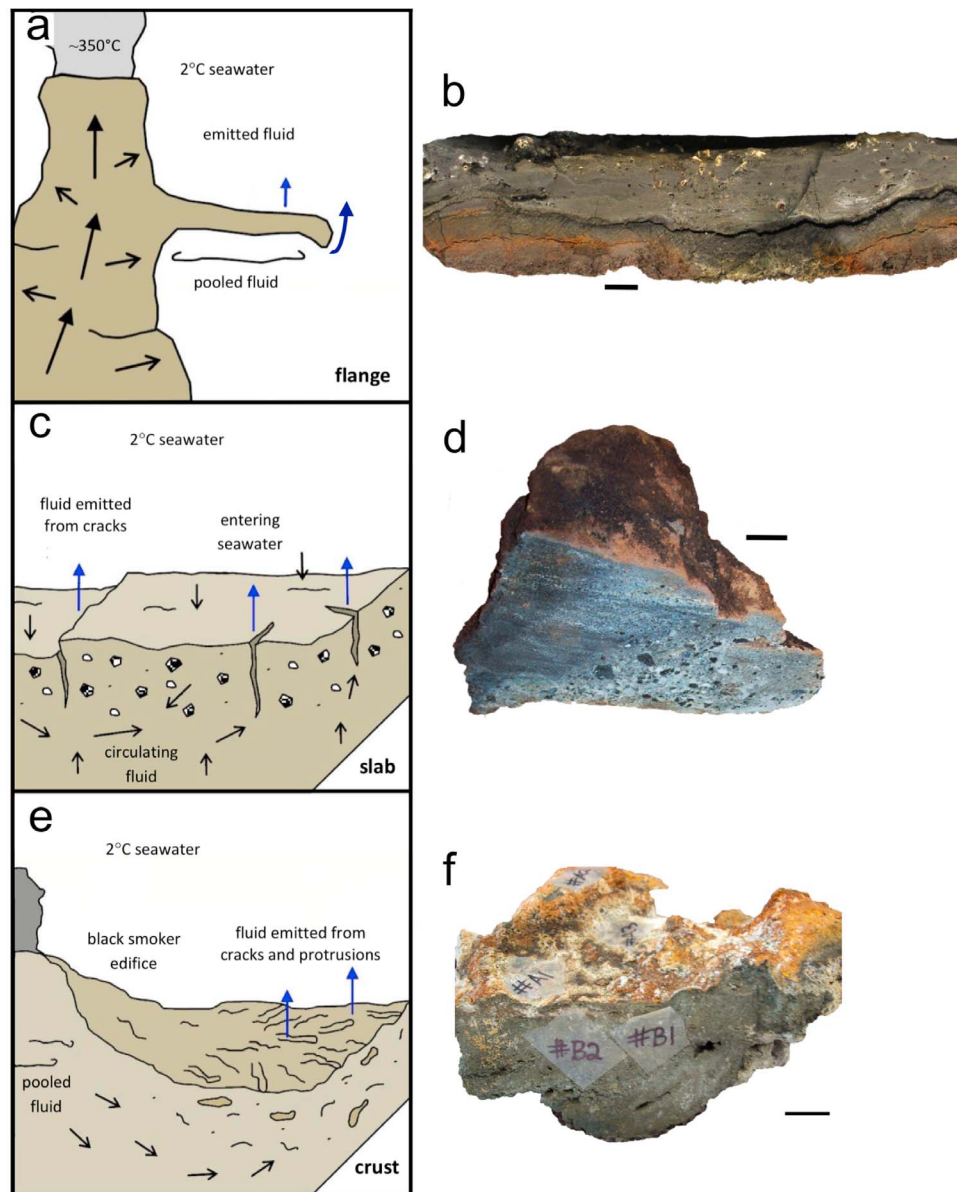
Figure 1. Diagrams illustrating the general structure and flow pathways within hydrothermal flanges, slabs, and crust, and photographs of a sample of each type used in this study. (a) Schematic depiction of a flange extending from the side of a larger chimney edifice. Fluid emitted from the side of the chimney will pool under the flange, percolate upwards through, and can overflow at the edge of, the flange. (b) Flange sample J2–286 from the Main Endeavour Vent Field. (c) Schematic depiction of a slab with circulating fluids. (d) Slab sample ALV2608-4-1 Pc 1 from the Lucky Strike Vent Field. (e) Schematic depiction of crust with fingerlike protrusions that is present on the slopes of the TAG black smoker edifice. (f) Crust sample ALV2179-1-1 showing locations where permeameter measurements were made, and where cores were subsequently taken. Scale bar in photographs is 2 cm.

flange, or overflow around the edge of the flange when the fluid flux exceeds the maximum amount that can percolate upwards through the flange [*Delaney et al.*, 1992; *Tivey et al.*, 1999]. As hydrothermal fluids overflow, mixing with seawater results in mineral precipitation along the flange edge, resulting in the lateral growth of the flange [*Delaney et al.*, 1992]. Deposition of silica within

flanges (e.g., at the Endeavour Segment) makes them more stable and able to attain large lateral extent [*Tivey et al.*, 1999]. In general, flanges are composed of sulfide minerals, barite and anhydrite, amorphous silica ± carbonates (calcite and aragonite) [*Peter and Scott*, 1988; *Delaney et al.*, 1992; *Tivey et al.*, 1999], with the presence of barite and

calcite also contributing to their structural integrity allowing them to attain large lateral extent.

[7] Flange samples for this study are from the Guaymas Basin in the Gulf of California and the Main Endeavour Vent Field (MEF) located along the Endeavour Segment on the northern portion of the Juan de Fuca Ridge. Guaymas Basin is notable for its rapid rate of sediment deposition and hydrothermal reactions between fluids and organic-rich sediments [*Von Damm et al.*, 1985]. As a result, fluids rich in CO_2 and barium result in calcite and barite being common constituents of vent deposits from this region [*Koski et al.*, 1985; *Peter and Scott*, 1988]. The MEF is atypical in that vent fluids are unusually enriched in methane and ammonia relative to vent fluids from other unsedimented mid-ocean ridges [*Lilley et al.*, 1993; *Butterfield et al.*, 1994]. High ammonia concentrations buffer pH, and result in significant saturation of sulfide minerals (particularly wurtzite) at higher temperatures than in systems that lack ammonia; the prevalence of late-stage amorphous silica in Endeavour vent deposits is attributed to precipitation from buffering of pH, as fluids cool via conduction ± mixing with seawater [*Tivey et al.*, 1999; *Kristall et al.*, 2006].

[8] Hydrothermal slabs (Figures 1c and 1d) are found at the Lucky Strike Vent Field along the Mid-Atlantic Ridge (MAR) at 37°N. The vent field is located within the central depression among three cones that make up the summit of a large ~50 km² seamount; the seamount is composed of lavas of variable age and flow morphology (vesicular lavas with no glass rinds and significant sediment cover versus more recent very fresh, glassy lavas) [*Langmuir et al.*, 1997], and extensive volcaniclastic deposits [*Eissen et al.*, 2003]. As described by *Eissen et al.* [2003], the volcaniclastic deposits are composed of highly vesicular glassy clasts, with accessory plagioclase clasts and more altered fragments, and the deposits are well stratified; mm- to cm-scale layering is attributed to emplacement by settling of suspended fragments from the water column. The Lucky Strike vent field consists of several actively venting deposits situated around a lava lake that is ~300 m in diameter, with the vent deposits surrounded by, and growing through, layered hydrothermally silicified volcaniclastic deposits (slab) [*Langmuir et al.*, 1997; *Rouxel et al.*, 2004]. The slab deposits contain abundant amorphous silica and clay as a rind on clasts and fragments, and filling interstices, with minor to trace barite and pyrite [*Langmuir et al.*, 1997; *Rouxel et al.*, 2004]. The amorphous silica, clay, barite

and pyrite likely precipitated during conductive cooling of mixtures of vent fluid and seawater as they percolated through the volcaniclastic deposits [e.g., *Tivey et al.*, 1999]. Compositions of diffuse fluids exiting from slabs in 1997, however, are consistent with seawater entering and circulating within the slab, with no evidence for mineral precipitation from the circulating fluids [*Cooper et al.*, 2000]. Because the compositions of sampled fluids could not explain the presence of amorphous silica, *Cooper et al.* [2000] hypothesized that the hydrothermal slab mineralogy and composition, with abundant amorphous silica present, likely reflects a previous phase of diffuse flow.

[9] Crust samples (Figures 1e and 1f) are from the TAG active mound along the MAR at 26°N. This vent field consists of a large circular mound, ~200 m in diameter, topped by a high-temperature black smoker complex [*Thompson et al.*, 1985]. Hydrothermal crust forms a cracked, plate-like layered surface on the slopes of this complex [e.g., *Tivey et al.*, 1995]. The crusts are composed of massive chalcopyrite and pyrite/marcasite. Some samples include small conduits up to a few millimeters in diameter, lined with either chalcopyrite or marcasite. Other crust samples include clasts of sulfide and oxide, consistent with formation from cementation of debris by later sulfide and silica [*Tivey et al.*, 1995]. Mineral textures and chemical composition of crust samples support formation from a fluid, similar in composition to black smoker fluids, pooled beneath the black smoker complex that percolated through debris, previously deposited sulfide layers, and small finger-like channels and cracks [*Tivey et al.*, 1995].

3. Permeability and Porosity Measurements

[10] Measurements were carried out on samples that include pieces of five flanges, four slabs, and one crust (Table 1). Because vent samples are typically quite heterogeneous, the protocol developed by *Zhu et al.* [2007] was followed. Permeability measurements were made along the surface of the different sides of the samples using a probe permeameter, the NER TinyPerm II™ (see Figure 1f where locations of 5 sites for sample ALV2179-1-1 are indicated). Five measurements were made at regularly spaced sites with about 3 to 6 sites along each sample side. A compilation of the mean values, ranging from 10^{-11} to 10^{-14} m², and their standard deviations are listed in Table 1. Samples vary in size, but all exceed 10 cm in lateral dimensions, and vary in

Table 1. Average Permeability and Porosity Data for Flange, Slab, and Crust Samples[a]

| Sample Core | Probe k ($\times 10^{-15}$ m^2) | | Core k ($\times 10^{-15}$ m^2) | | | | | | Core ϕ (%) | | | |
| | | | 1.4 MPa | | 2.1 MPa | | 2.7 MPa | | 2.1 MPa | | 2.7 MPa | |
	k	2σ	k	2σ	k	2σ	k	2σ	ϕ	2σ	ϕ	2σ
Guaymas Basin Flanges												
ALV 3517-R1												
D1[b]	3230.4	±3.6	59.1	±0.3	55.1	±0.3	52.9	±0.4	2.3	±3.3	21.6	±3.1
D3[c]	1884.9	±4.5	32.0	±0.3	29.5	±0.2	28.0	±0.2	2.8	±4.4	19.8	±4.0
ALV 3521-R2												
A2[b]	29981.0	±4.5	1425.8	±3.2	1420.6	±3.3	1414.2	±13.0	11.5	±0.1	40.5	±0.2
Ex 1[b]	–		1311.7	±3.3	1243.4	±3.8	1213.1	±8.5	2.1	±0.4	44.8	±0.2
Ex 2[b]	–		969.7	±4.2	954.7	±5.4	953.8	±2.0	5.6	±0.4	44.7	±0.3
MEF Flanges												
ALV 2927-3												
B1[b]	2193.3	±2.5	1930.6	±10.8	1889.1	±12.7	1863.5	±6.2	38.2	±0.1	37.9	±0.1
1	–		*1950.2*	–	*1717.7*	–	*1595.6*	–	*41.8*	–	*39.6*	–
2	–		155.6	–	148.7	–	145.0	–	32.7	–	29.5	–
3	–		994.2	–	967.3	–	948.7	–	40.7	–	38.2	–
ALV 2415-1B												
A1[c]	*1694.3*	*±3.8*	*56.5*	*±0.3*	*55.4*	*±0.4*	*54.7*	*±0.5*	*20.2*	*±1.2*	*20.5*	*±0.4*
B1	9704.2	±3.3	1594.6	±4.8	1552.3	±3.4	1514.3	±4.7	31.2	±0.3	30.9	±0.4
1	–		46.1	–	40.5	–	36.5	–	17.1	–	15.3	–
2	–		5.3	–	3.5	–	2.6	–	19.2	–	17.2	–
J2-286												
A1[b]	2062.0	±3.7	1.3	±0.1	0.5	±0.02	0.2	±0.02	20.7	±0.1	20.5	±0.3
A3	4181.9	±4.3	279.4	±1.3	233.1	±1.3	196.0	±1.6	25.3	±1.6	25.3	±0.9
C2-1[b]	46446.3	±3.8	0.8	±0.04	0.8	±0.02	0.7	±0.03	27.2	±0.5	27.3	±0.3
C2-2	–		1.3	±0.04	1.2	±0.02	1.2	±0.1	24.1	±0.2	24.2	±0.4
C3-1[c]	79602.4	±3.2	162.9	±0.4	146.0	±1.3	138.3	±1.4	27.6	±4.5	27.8	±3.4
C3-2	–		49.9	±0.5	48.7	±0.2	48.3	±0.3	21.2	±1.1	20.7	±1.5
C4[b]	94066.3	±2.8	18.7	±0.1	17.7	±0.2	17.0	±0.1	17.7	±2.4	19.9	±2.1
Lucky Strike Slabs												
ALV 2608-3-3												
B2	*1960.4*	*±4.4*	*2744.7*	*±13.5*	*2737.1*	*±11.9*	*2746.1*	*±5.6*	*42.9*	*±0.4*	*42.5*	*±0.3*
C1	*1051.5*	*±4.5*	*1445.3*	*±5.9*	*1447.1*	*±3.1*	*1436.6*	*±3.5*	*29.2*	*±0.3*	*28.8*	*±0.3*
ALV 2608-4-1, Pc 1												
A1	*816.8*	*±3.9*	*787.8*	*±2.7*	*740.6*	*±3.4*	*706.5*	*±1.1*	*34.9*	*±0.2*	*34.8*	*±0.3*
C1-1	428.4	±3.9	530.0	±1.9	486.7	±0.4	461.0	±2.3	37.2	±1.0	36.5	±1.3
C1-2	–		757.9	±8.2	655.1	±5.1	604.9	±4.0	46.4	±0.8	46.3	±0.4
C3-1[b]	1196.4	±3.8	28.1	±0.2	24.1	±0.2	22.2	±0.2	35.0	±0.9	34.8	±0.3
C3-2	–		120.3	±1.2	111.7	±1.1	106.9	±0.8	37.2	±0.8	37.1	±0.6
ALV 2608-4-1, Pc 2												
A3	*2319.9*	*±4.6*	*2056.1*	*±4.5*	*2016.9*	*±6.5*	*1994.5*	*±5.5*	*39.8*	*±0.3*	*39.6*	*±0.1*
B3	1176.4	±4.0	561.6	±2.2	538.3	±2.8	523.0	±0.9	43.1	±0.1	42.8	±0.2
1	–		5475.2	–	5023.6	–	4885.3	–	45.6	–	44.1	–
2	–		661.4	–	574.6	–	534.1	–	48.0	–	46.3	–
4	–		962.2	–	695.1	–	528.8	–	44.0	–	42.4	–
JAS 177-2-1												
A2[b]	3975.9	±4.1	198.5	±1.8	170.4	±2.1	152.1	±1.5	46.1	±0.4	45.7	±0.4
B1[b]	*2729.9*	*±3.5*	*1827.7*	*±3.8*	*1774.8*	*±2.9*	*1745.9*	*±4.5*	*38.8*	*±1.5*	*38.9*	*±1.2*
B2[b]	*9435.7*	*±3.2*	*2998.6*	*±13.7*	*2954.2*	*±11.8*	*2898.5*	*±4.1*	*41.2*	*±1.8*	*41.0*	*±1.7*
C2[b]	*69963.2*	*±3.9*	*194.1*	*±0.5*	*192.1*	*±0.6*	*191.9*	*±0.2*	*41.2*	*±3.7*	*39.5*	*±3.4*
TAG Crust												
ALV 2179-1-1												
A1[b]	13897.7	±3.0	605.0	±2.8	575.9	±0.7	560.7	±1.2	36.9	±3.1	35.3	±4.3
A2[b]	5234.4	±3.6	1106.7	±6.9	1079.1	±5.5	1062.7	±2.9	37.9	±5.0	37.8	±3.2
A3[c]	23030.1	±1.4	927.9	±4.4	887.3	±4.7	863.2	±4.7	38.4	±4.5	37.2	±2.5
B2	*1464.2*	*±3.4*	*1487.5*	*±5.0*	*1476.5*	*±9.7*	*1462.7*	*±4.6*	*43.2*	*±0.2*	*42.4*	*±0.4*

thickness (vertical dimension) from ∼2.5 cm to ∼14 cm. These data provide a quantitative measure of permeability heterogeneity within the samples. Comparison of permeability values obtained from different sides of each sample show that measurements oriented parallel to layering were predominantly on the order of 10^{-12} m². Measurements taken perpendicular to layering yielded a much broader range of values, with the mean much lower than 10^{-12} m².

[11] Following probe measurements, 25.4 mm (one-inch) diameter cores of varying lengths were taken from different sides of each sample, primarily at sites from which probe permeameter measurements had been made. Cores were taken both parallel and perpendicular to layering within each of the samples whenever possible in order to better quantify permeability anisotropy. Some of the cores broke into smaller pieces because of the presence of cracks or zones of high porosity, in which case each coherent section was treated as a separate core. The ends of some cores were trimmed to create parallel upper and lower core surfaces. In total, 40 cores with lengths varying from 1 to 6 cm were obtained with 9 cores oriented parallel, and 31 cores perpendicular, to layering. Using these cylindrical cores, permeability was measured along the axial direction with a nitrogen permeameter, the UltraPerm™ 400. Sample porosity was also measured for the cores using a helium porosimeter, the UltraPore™ 300. Both the N_2-permeameter and He-porosimeter allow for the application of a confining pressure up to 4 MPa [Zhu et al., 2007]. During permeability measurements, cylindrical cores were subjected to a confining pressure starting at 0.5 MPa, which then gradually increased to 2.7 MPa (during porosity measurements, confining pressures ranged from 2.1 to 3.1 MPa). The confining pressure was applied over eight increasing intervals with five measurements made during each pressure step. The stepwise application of the confining pressure and the multiple permeability measurements at each confining pressure enabled us to gauge the effect of pressure on the pore structure [e.g., Walsh, 1965]. Permeability measurements were also taken while the confining pressure was incrementally removed from the sample (i.e., unloading). In general, both the permeability and

porosity decreased slightly with increases in confining pressure, likely due to crack closure [e.g., Walsh, 1965]. The permeability values obtained during unloading agree well with the values obtained during loading, indicating that the pressure effect is mostly reversible with negligible permanent damage introduced during pressurization.

[12] The permeability reduction in all cores became negligible as the applied confining pressure increased from 2.1 MPa (300 psi) to 3.1 MPa (450 psi). Thus, we used the measurements taken at 2.1 MPa for analyses in this study. Table 1 shows the average permeability and porosity values at 2.1 MPa and the respective average probe permeability measurements. The majority of the cores measured had corresponding probe measurements, but additional measurements were also conducted on several cores taken where no probe permeameter measurements were made. Comparison between the permeability values obtained by TinyPerm II and those obtained by UltraPerm™ 400 indicate that for the same sample, probe permeability is consistently higher (Table 1). Part of the difference is due to the application of the confining pressure during core permeability measurements. Another reason is that flow measured by the TinyPerm II is not directionally restricted, so the values obtained are a representation of a near surface volume average, whereas UltraPerm™ 400 provides an axial permeability of a cylindrical core [Zhu et al., 2007]. In addition, probe measurements were sometimes made on surfaces that were trimmed off of the cores (because the core measurements need to be made on cylindrical cores with parallel upper and lower surfaces). Notwithstanding these differences, data of the core samples reinforce the observation that within each sample, the parallel-to-layering permeability values do not show significant variability. The parallel-to-layering cores all had relatively high permeabilities on the order of 10^{-12} m² (with standard deviation $2\sigma = 7.3 \times 10^{-15}$ m²). In contrast, the perpendicular-to-layering permeability values range over several orders of magnitude, from 10^{-16} to 10^{-12} m², with the mean much lower than 10^{-12} m² (with standard deviation $2\sigma = 1.7 \times 10^{-15}$ m²).

[13] The average porosities of the parallel-to-layering cores (ranging from 30 to 40%) are also higher

---

Notes to Table 1:

   [a]Average probe permeability, core permeability, and porosity and 2σ values for flange, slab, and crust samples. Additional data for analyses were taken from cores without corresponding probe permeability measurements. Italicized text represents parallel-to-layering data.
   [b]Cores that had ≥0.5 cm cut from the end of the core from which the probe permeability measurement was taken.
   [c]Cores from which <0.5 cm of material was removed, yet the removed portion consisted of a high porosity layer, significantly more porous than the bulk of the sample.
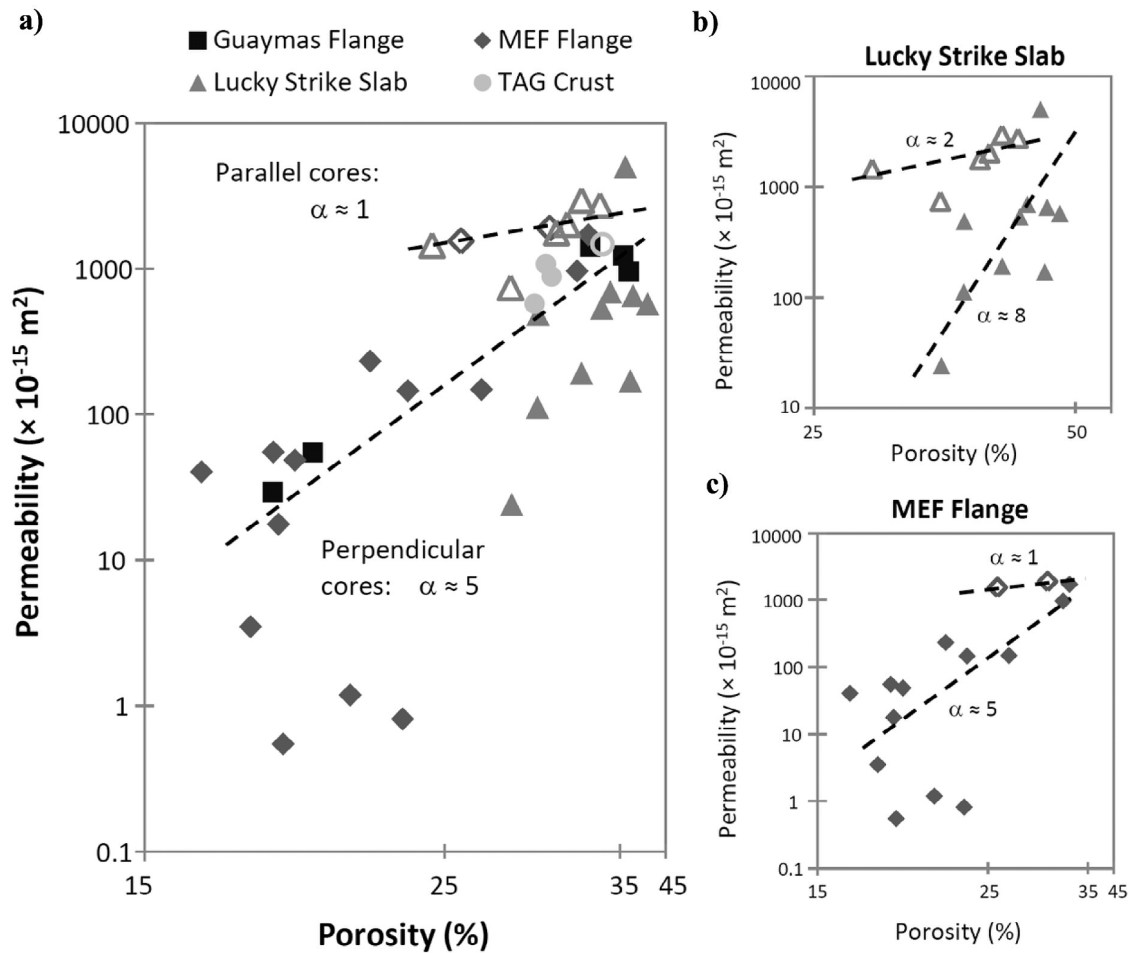
Figure 2. (a) Permeability versus porosity data for all of the cores. In general, permeability values for cores taken parallel-to-layering, empty symbols, are higher ($\approx 10^{-12}$ m^2) than for cores taken perpendicular-to-layering ($10^{-16}-10^{-12}$ m^2). Differences in permeability as a function of porosity can be best fit by power law relationships (black dashed lines), with a power law exponent of $\alpha \approx 1$ (or 2) for the parallel-to-layering cores and $\alpha \approx 5$ (or 8) for the perpendicular-to-layering cores. Symbol shape denotes location of sample origin: square = Guaymas Basin, diamond = MEF, triangle = Lucky Strike, and circle = TAG. (b) Permeability versus porosity for only Lucky Strike cores with power law relationships identified. (c) Permeability versus porosity for MEF cores with power law relationships labeled.

than those of the perpendicular-to-layering ones (ranging from 20 to 40%). Based on these permeability and porosity values, we separated the cores into two groups: cores with axes oriented parallel-to-layering and cores with axes oriented perpendicular-to-layering (Figure 2).

[14] Power law relationships have often been used to characterize permeability as a function of porosity [e.g., *Turcotte and Schubert*, 1982; *Zhu et al.*, 1999, 2007]:

$$k \propto \phi^{\alpha} \qquad (1)$$

The evolution of permeability-porosity relationship (EPPR) can be depicted using this frame work,

where the exponent α characterizes the dependence of permeability on changes in porosity; for a given amount of porosity change, higher α value means a larger permeability change [*Zhu et al.*, 2007]. From Figure 2, two distinct trends of EPPRs are evident for the parallel-to-layering and perpendicular-to-layering cores: $\alpha \approx 1-2$ for the parallel-to-layering cores, and $\alpha \approx 5-8$ for the perpendicular-to-layering cores.

[15] Permeability depends closely on pore connectivity and pore geometry. The exponent α represents an averaging effect of generally complex pore structure on permeability. To correctly interpret EPPRs observed in this study, it is critical to relate

the power law relationships to the actual pore evolution processes [*Bernabé et al.*, 2003; *Zhu et al.*, 2007]. Following the permeability and porosity measurements, thin sections were made from a large subset (total of 26) of the cores, both parallel and perpendicular to layers (see Table 2).

4. Microstructural Analyses

[16] Microstructural analyses using reflected and transmitted light petrography were conducted on thin sections to identify pore evolution processes. Permeability-porosity data for samples from which thin sections were obtained are shown in Figure 3. Data are grouped according to vent field and sample type: Guaymas flanges, MEF flanges, Lucky Strike slabs, and TAG crust. A summary of observations for each thin section is provided in Table 2.

4.1. Guaymas Flanges

[17] The flanges have been separated into two groups, carbonate-dominated samples from the Guaymas Basin, and sulfide-dominated samples from the MEF. The permeability and porosity values of the two flange samples from Guaymas, ALV3517-R1 and ALV3521-R2 (Figures 4a and 4b), differ considerably (Figure 3a). For each sample, one thin section was cut axially through one core, and a second was cut transversely through another core (Table 2). For sample ALV3517-R1, the axial cut (Core D1) exhibits a layer of coarse-grained (≈1 to 2 mm) calcite at the base of the core. Trace fine-grained pyrrhotite (15 × 150 μm) and sphalerite (≈50 μm) are present along calcite grain boundaries. Fine- to medium-grained calcite (≈100 to 400 μm) comprises the bulk of the rest of the flange layer above, and fills pore space between, the coarser-grains. Radial splays (up to 600 μm × 25 μm) of stevensite are abundant, coprecipitated with the fine- to medium-grained calcite. Pore space is limited (∼20%), as isolated pores between clusters of both calcite and stevensite, with smaller pores (100 to 300 μm) near the top and larger pores (400 to 1000 μm) near the base of the core. There is little to no pore connectivity exposed in the thin section. The transverse section (Core D3), taken through a region of the core near the transition from coarser- to finer-grained calcite, also reveals limited pore space and a lack of pore connectivity. Tight packing of calcite and stevensite likely inhibited flow, accounting for the low permeability values measured.

[18] For sample ALV3521-R2, which has significantly higher permeability and porosity values (Table 1 and Figure 3a), the axial cut (Core Ex 1) exhibits pockets of coarse-grained (500 to 2000 μm) calcite at the base of the core, with the majority of the core composed of finer-grained (40 to 100 μm) calcite intergrown with splays (200 to 2000 μm long, 20 to 200 μm wide), of stevensite. Isolated pores 100 to 200 μm in size are present throughout, with a few very large (500 to 1000 μm) pores present. The transverse section (Core Ex 2) reveals textures very similar to those in the thin section from core Ex 1 (Table 2). In ALV3521-R2, grain size and packing is more variable, and there is more pore space (core porosity is ∼45%), than in sample ALV3517-R1 (Table 2).

[19] The Guaymas flange samples likely evolved from an initial fine- to medium-grained calcite and stevensite matrix formed as fluids overflowed and mixed with seawater, similar to initial emplacement of "stage 1" black smoker chimney walls [*Haymon*, 1983; *Goldfarb et al.*, 1983]. Later infilling calcite, stevensite and sulfide minerals then precipitated interstitially as fluids from the underlying pool percolated upwards cross a steep thermal gradient and cooled, and mixed with variable amounts of seawater, again similar to processes proposed for black smoker chimneys. Coarser-grained calcite precipitated on the underside of the flange from a pooled CO_2-rich, high temperature fluid [*Peter and Scott*, 1988; *Von Damm et al.*, 1985]. It is possible that the lower porosity textures observed in sample ALV3517-R1, which has the lower permeability of the two Guaymas samples, represents a pore structure that evolved from a pore structure similar to that of ALV3521-R2, with the porosity and permeability decrease from precipitation within preexisting pore space.

4.2. MEF Flanges

[20] The MEF flange samples are composed dominantly of sulfide minerals, with lesser amorphous silica, trace clay, and an absence of carbonate. Nine thin sections were made from three samples: ALV2927–3 (Figures 4c, 4d, 4f, and 4g; 3 thin sections), ALV2415–1B (Figure 4h; 2 thin sections), and J2–286 (Figures 4e and 4i; 4 thin sections) (Figure 3b). Seven of the nine thin sections are from cores oriented perpendicular to layering, with five of these sections cut axially to cross the different layers; two sections were cut along the radial direction of the cylindrical core, parallel to layering. The other two thin sections are from

Table 2. Summary of Microstructural Observations for Flange, Slab and Crust Thin Sections[a]

Sample and Section	k ($\times 10^{-15}$ m^2)	ϕ (%)	Minerals Present	Grain Packing and Size	Pore Size	Pore Connectivity	Channel Width Min-Max (Average)	Section Cut[b]
Guaymas Basin Flanges								
ALV 3517-R1								
D1	55.1	22.1	ca, st (po, sp, cb)	tight; 100 to 400 μm ca + st, trace po, sp, cb; 1 to 2 mm ca at flange base	60 to 1000 μm isolated pores, larger near flange base	low	<20 μm (10 μm)	2
D3	29.5	20.2	ca, st (po, sp, cb)	tight; patches of 200 to 500 μm ca, but most 50 to 75 μm + st, trace po, sp, cb	isolated 100 to 500 μm pores; most 150 μm	moderate	<40 μm (20 μm)	3
ALV 3521-R2								
Ex 1	1243.4	45.3	ca, st (am si, po, sp)	tight; 40 to 100 μm ca + st; patches of coarser 500 to 2000 μm ca + st	100–200 μm pores, regularly distributed; some 500 to 1000 μm pores	moderate	<40 μm (10 μm)	2
Ex 2	954.7	45.9	ca, st (ba, po, sp)	tight; 20 to 50μm ca +st; patches of coarser 500 to 1000 μm ca + st	20–150 μm pores regularly distributed, some 500 to 2000 μm pores	moderate	<40 μm (10 μm)	3
MEF Flanges								
ALV 2927-3								
B1	1889.1	38.2	py, wz (po, cp, cl)	loose; 20 to 300 μm py, wz, minor cp, po, trace cl	irregularly shaped pores 40–800 μm; smaller isolated pores	high	10–80 μm (20 μm)	1
3	967.3	40.7	py, wz (po, cp, cl, am si)	moderate; 5 to 100 μm py, wz, minor cp, po, trace cl; 10 to 20 μm am si rind in some portions	irregularly shaped pores 20–400 μm; minor isolated pores	high	10–180 μm (40 μm)	3
2	148.7	32.7	py, wz (po, cp, Fe ox, am si)	tight-moderate; 5 to 200 μm py, wz minor po, cp, cl; Fe ox from alteration of po; 20 μm am si rind in upper core	irregularly shaped pores 30–400 μm; minor isolated pores	moderate	10–70 μm (20 μm)	2
ALV 2415-1B								
B1	1552.3	31.2	py, mc, am si, cp, wz	moderate; 10 to 300 μm py, mc, wz, cp, fossil worm casts, 40 μm am si rind	pores 30 to 600 μm; some am si restricting pore channels	moderate (high in 1 layer)	10–50 μm (20 μm) (20–130 μm (30 μm))	1
A1	55.4	20.2	py, mc, wz, am si, cp	tight; 10–150 μm py, mc, wz, cp, fossil worm casts, am si as 40 μm rind in upper core	pores 30–400 μm; abundant am si restricting pore channels	low	10–50 μm (20 μm)	2
J2-286								
C3-1	146.0	27.6	py, wz, po, cb (Fe ox)	tight; 10 to 150 μm py, wz near core top; 200 to 3000 μm po and 500 μm cb near core bottom; Fe ox replaces po	pores 50 to 600 μm, larger near core bottom (flange underside); cracks (up to 200 μm wide) present	moderate	10–200 μm (40 μm)	2

Table 2. (continued)

Sample and Section	k (× 10⁻¹⁵ m²)	ϕ (%)	Minerals Present	Grain Packing and Size	Pore Size	Pore Connectivity	Channel Width Min-Max (Average)	Section Cut[b]
C3–2	48.7	21.2	py, am si (wz, mc, cp)	tight; 10 to 200 μm py (wz, mc, cp) w/5 to 40 μm am si rind, thicker at top	pores 40–400 μm; fossil tube worm casts (2 mm diameter); 1.5 mm pores near casts	moderate	10–50 μm (20 μm)	2
C2–1	0.8	27.2	py, mc, wz (po, Fe ox)	moderate; 10 to 200 μm py, mc, wz; Fe ox along grain boundaries	pores 20–200 μm; fossil tube worm casts (80 to 400 μm)	moderate	5–50 μm (15 μm)	3
A1	0.5	20.7	py, mc, am si (wz, po)	tight; 10 to 175 μm py, mc w/ubiquitous 20 μm am si rind	pores 10–400 μm; fragments of tube worm casts	low	5–100 μm (10 μm)	2
Lucky Strike Slabs								
ALV 2608-3-3								
B2	2737.1	42.9	gl (pl, am si, py)	loose/variable packing; 50 to 2000 μm gl (pl) clasts w/20 μm am si layer; am si + cl in interstices; trace py	very porous; pores 50–1000 μm	high	10–400 μm (50 μm)	1
C1	1447.1	29.2	gl, am si (pl, py)	moderate, but variable; 30 to 1000 μm gl (pl) clasts w/20 μm am si +clay; trace py	very porous, pores 50 to 600 μm; connectivity lost to am si	moderate	10–100 μm (30 μm)	1
ALV 2608-4-1, Pc 1								
A1	740.6	34.9	gl, am si, cl (pl)	moderate to tight; 50 to 500 μm gl clasts and am si ± cl	pores 10–600 μm; some channels blocked by am si ± cl	low	10–80 μm (15 μm)	1
C3-2	111.7	37.2	gl, am si, cl (pl)	moderate; 50 to 500 μm gl clasts, interstitial cl, 10 μm am si layer	pores 20–800 μm; few channels blocked by am si ± cl	moderate	10–80 μm (40 μm)	2
C3-1	24.1	35.0	gl, am si, cl (pl)	moderate; 80 to 3000 μm gl (pl) clasts; in parts, cl fills all interstices	pores 10–1000 μm; few channels blocked by am si ± cl	moderate (very low in 1 layer)	10–200 μm (50 μm) (<40 μm (5 μm))	2
ALV 2608-4-1, Pc 2								
A3	2016.9	39.8	gl (am si, cl, pl)	moderate; 60 to 800 (some 3000) μm gl clasts w/ am si rind	very porous; pores 50–1000 μm	high	10–200 μm (40 μm)	1
2	574.6	48.0	gl (am si, cl, pl)	moderate; 100 to 800 (some 4000) μm gl (pl) clasts w/ 5 μm am si rind	very porous; pores 50–1000 μm; minor am si + cl	high	10–200 μm (40 μm)	2
B3	538.3	43.1	gl (am si, cl, pl)	moderate; 100 to 800 (some 2000 to 3000) μm gl (pl) clasts	very porous; pores 50–1000 μm; minor am si + cl	high	10–200 μm (40 μm)	2
JAS 177-2-1								
B2	2954.2	41.2	gl (am si, cl, pl)	loose; 30 to 900 μm gl clasts w/am si+cl	very porous; pores 50–800 μm; minor am si ± cl	high	10–400 μm (50 μm)	1
B1	1774.8	38.8	gl (am si, cl, pl)	loose; 30 to 900 μm gl clasts w/am si+cl	very porous; pores 50–800 μm; minor am si ± cl	high	10–400 μm (50 μm)	1
A2	170.4	46.1	gl, pl (am si, cl)	loose; 30 to 900 (some 3000) μm gl (pl) clasts w/am si+cl	variable; pores 20–650 μm; areas of high am si + cl	high	20–350 μm (30 μm)	2

Table 2. (continued)

Sample and Section	k ($\times 10^{-15}$ m^2)	ϕ (%)	Minerals Present	Grain Packing and Size	Pore Size	Pore Connectivity	Channel Width Min-Max (Average)	Section Cut[b]
TAG Crust								
ALV 2179-1-1								
B2	1476.5	43.2	cp, py/mc (sp)	moderate; 20 to 300 μm cp, minor py/mc	pores 40 to 400 μm; fossil tube worm casts (200 μm diameter)	high	10–150 μm (60 μm)	1
A1	575.9	36.9	cp, py/mc (sp)	moderate; 20 to 500 μm cp, minor py/mc	pores 30–200 μm; fossil tube worm casts (200 μm diameter); cracks (40 to 80 μm wide)	high	10–80 μm (30 μm) (except cracks)	3

[a]Sample permeability is likely controlled by least permeable layers. Mineral abbreviations: am si, amorphous silica; ba, barite; ca, calcite; cb, cubanite; cp, chalcopyrite; cl, clay; Fe ox, Fe oxide; gl, glass; mc, marcasite; pl, plagioclase; po, pyrrhotite; py, pyrite; sp, sphalerite; st, stevensite; and wz, wurtzite.
[b]Numbered as follows: 1, across layering cut of parallel-to-layering core; 2, across layering cut of perpendicular-to-layering core; 3, parallel to layering cut of perpendicular-to-layering core (see Figure 3e).

cylindrical cores oriented parallel to layering, and were cut along the radial direction to cross the different layers. The thin sections oriented perpendicular-to-layering exhibit the full range of textures in each sample.

[21] The thin section from the highest permeability core, ALV2927–3 core B1 (Figure 4d), reveals layers composed of fine- to medium-grained wurtzite and pyrite (20 to 300 μm), with minor fine- to medium-grained chalcopyrite and pyrrhotite, and trace clay. Differences in grain size and packing distinguish one layer from another, with different grain packing resulting in a range of pore connectivity throughout the sample. For example, one layer is particularly porous with well-connected pores with pore throat-size averaging 80 μm in width (Figure 4f). Pore connectivity in other layers is not as high, though grain packing is loose (i.e., grains are not touching and instead are rimmed with pore space; Figure 4g). The thin section from core 3, a core with lower permeability but higher porosity, reveals only one layer (because it was cut parallel to layering), and thus, likely is not representative of the entire core. The layer is similar in mineral content, packing, and pore connectivity to the layer of core B1 that exhibits the highest pore connectivity, but with much finer grain size, and, in patches, a 10 to 20 μm rind of amorphous silica coats sulfides. The thin section from ALV2927–3 core 2 reveals layers and textures very similar to those in the thin section from core B1 of the same sample, except that significant pyrrhotite has been altered to Fe-oxide, and upper layers of the core exhibit a 20 μm rind of amorphous silica. As a result, pore connectivity in some layers of core 2 is very low.

[22] Thin sections from sample ALV2415–1B cores B1 and A1 both comprise several layers. The thin section from core A1 is composed of pyrite, with minor wurtzite, marcasite, chalcopyrite, and variable amounts of amorphous silica. Fossil tube worm casts (1.5 mm diameter) and fragments of casts are present near the top of the core, rimmed with a layer of late amorphous silica (Figure 4h). Amorphous silica is least abundant at the base of the core, and greatest near the top of the flange. In the 2 dimensional section, interconnected pores are present only in layers where the sulfide minerals are loosely packed (not touching one another).

[23] The thin section from ALV2415–1B core B1 shows similar mineral content and texture, and variable amounts of late-stage amorphous silica are present as a 40 μm rind. Abundant fossil worm
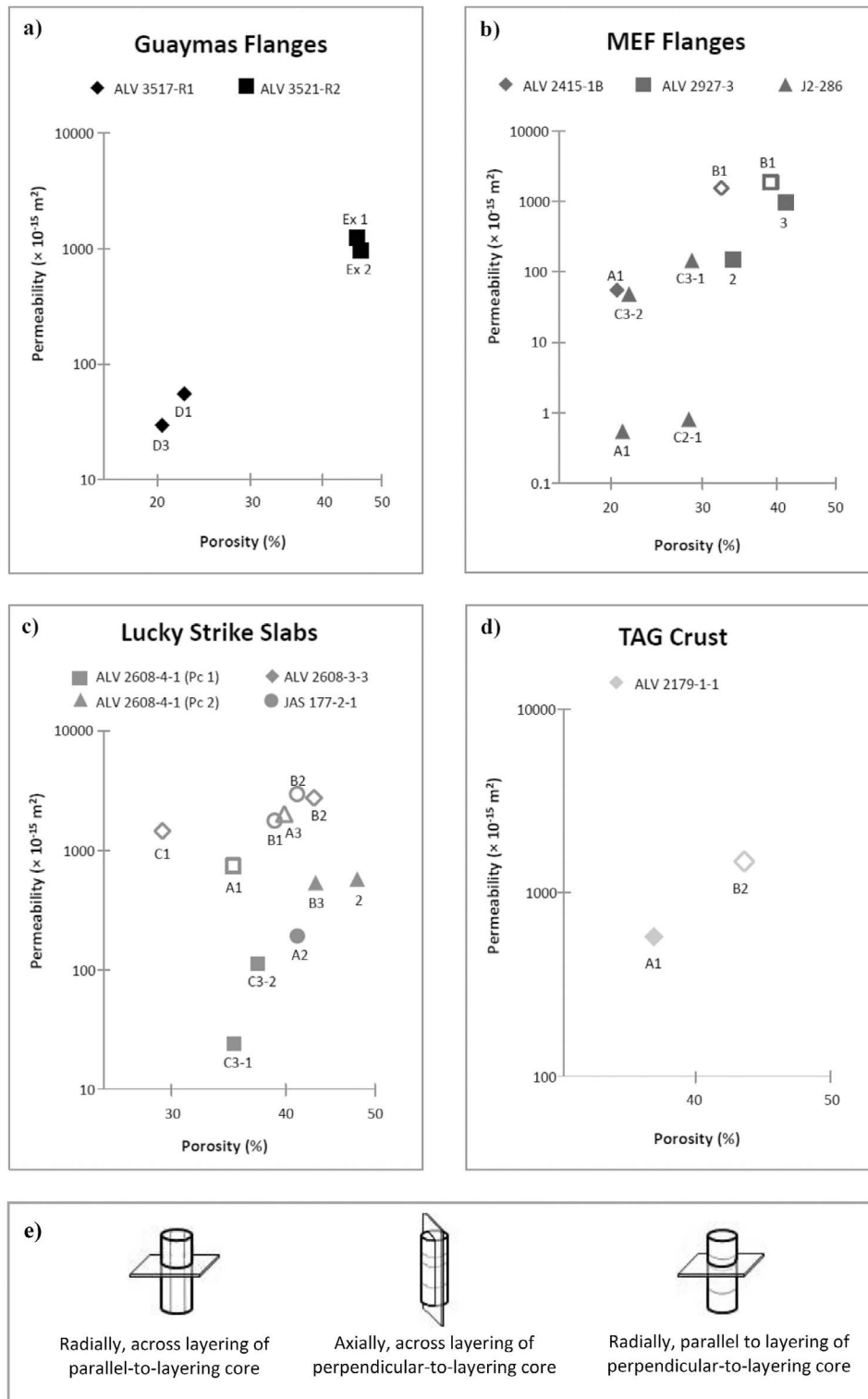
Figure 3. Permeability and porosity data for cores from which thin sections were obtained for microstructural analyses. Different samples from each location are marked by differently shaped symbols, with empty symbols denoting parallel-to-layering cores. (a) Guaymas Basin flange data, (b) MEF flange data, (c) Lucky Strike slab data, and (d) TAG crust data. (e) Orientation of thin section cuts from cores relative to sample layering.
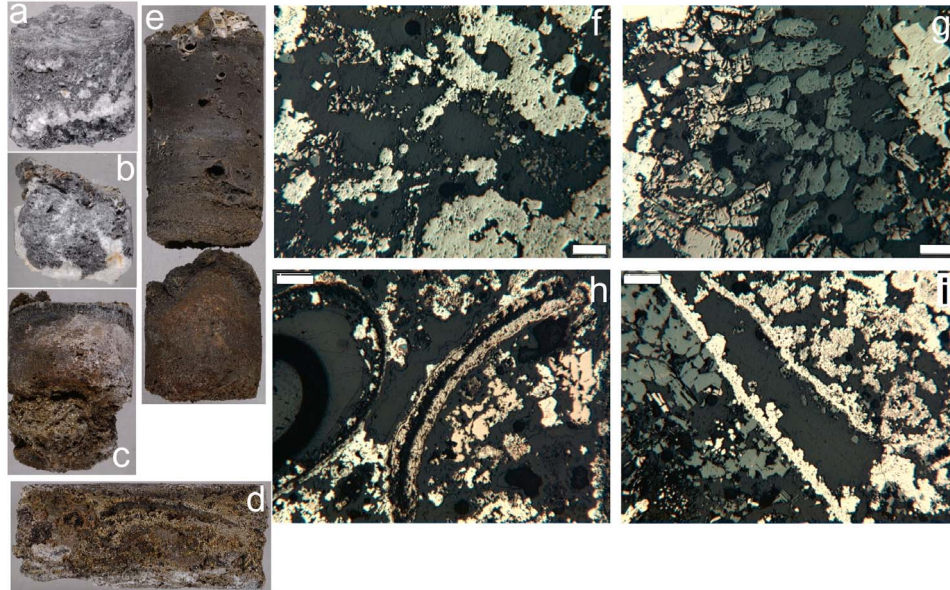
Figure 4. Flange cores (25.4 mm in diameter) and reflected light photomicrographs from flange core thin sections. (a) Guaymas flange ALV3517-R1 Core D1 and (b) Guaymas flange ALV3521-R2 Core Ex 2. Note coarse calcite at base of cores (undersides of flanges). (c) Main Endeavour Field flange ALV2927–3 Core A2, taken perpendicular to layering, and (d) ALV2927–3 Core B1, taken parallel to layering. (e) Main Endeavour Vent Field flange sample J2–286 Core 3; thin section 3–1 was made from the lower portion of the core and flange, and thin section 3–2 from the upper part of the core and flange. (f and g) Reflected light images of thin section from ALV2927–3 Core B1 taken of layers that exhibit different porosities. Scale bars are 200 μm. Dark gray and black is pore space, lighter gray is wurtzite, yellow is pyrite/marcasite, brownish blades are pyrrhotite. (h) Reflected light image showing fragments of mineralized tube worm casts in the thin section from Main Endeavour Flange sample ALV2415–1B Core A1. The image is from near the top of the core. Dark gray is either pore space or a gel-like coating of amorphous silica on sulfide surfaces, yellow is pyrite/marcasite, and gold is chalcopyrite. Scale bar is 200 μm. (i) Reflected light image showing open $\sim$200 μm crack (dark gray is pore space), lined with pyrite (yellow) and minor wurtzite (lighter gray), from the top of the thin section made from J2–286 Core 3–1. Scale bar is 200 μm.

casts ($\sim$1 mm diameter) and fragments of casts are present. Several very large pores (up to 1 mm) are present in a layer that includes fossil worm casts. Similar to ALV2927–3 core B1, the highest permeability layer of ALV2415–1B core B1 likely exerts the greatest control on the overall permeability of the core.

[24] For sample J2–286, four thin sections were made from cores oriented perpendicular to layering. The thin section from core C3–1 (see Figure 4e) reveals layers that differ from one another in mineral content, grain shape and size, porosity, and packing. The layer at the base of the core is composed of coarse-grained pyrrhotite (200 μm wide, 3000 μm long) and cubanite (500 μm), with large pore spaces ($\sim$300 μm) adjacent to large pyrrhotite grains. Mid- and upper-layers of the core are composed of fine- to medium-grained (10 to 150 μm) resorbed pyrrhotite (altered to Fe-oxide), pyrite and wurtzite. Open and partially filled (e.g., lined with pyrite; Figure 4i) cracks are present. The thin

section from core C3–2 (transecting the upper part of the flange; Figure 4e) reveals layers that are composed primarily of pyrite and minor amounts of wurtzite and marcasite, coated with a 5 to 40 μm rind of amorphous silica, thicker near the top of the flange. Precipitation of amorphous silica as a rind on sulfide minerals has reduced pore throat size, thus restricting flow. Fossil tube worm casts are present in one layer, with the tubes 50% filled by later pyrite and amorphous silica spherules. The thin section from core A1 is similar to that from core C3–2. In the majority of the layers in core A1, abundant amorphous silica is present as a ubiquitous 20 μm rind, blocking spaces between grains and filling pre-existing pore space. The few remaining pores are isolated, with no connectivity apparent in the thin section. The thin section from core C2–1 differs from the other thin sections in that it was taken through one of the core's layers rather than parallel to the axis of the core. The layer exhibits narrow pore throats that are moderately well connected. Amorphous silica is absent, Fe-oxide

occurs along grain boundaries, and the fossil tube worm casts are much smaller in size (200 μm versus 2 mm) than in other parts of this sample. We speculate that the low permeability measured for this core may well be indicative of the presence of substantial amorphous silica elsewhere in the core, in a layer that was not transected by the thin section.

[25] Microstructures observed in the thin sections provide insights into the evolution of porosity and permeability during flange growth. The presence of coarser-grained sulfide along the base of the flanges can be explained by precipitation from the underlying pooled fluid onto the underside of the flange under relatively constant conditions, similar to precipitation of coarse-grained chalcopyrite along black smoker conduits [e.g., *Haymon*, 1983; *Goldfarb et al.*, 1983]. Pore space between these coarse sulfide grains accommodates the upward migration of hot fluids. Fine- to medium-grained upper- and mid-layers of flanges likely formed initially from mixing of overflowing vent fluids and seawater [*Delaney et al.*, 1992]. Upward migration and conductive cooling of vent fluids that had been pooled beneath the flange, and vent fluid/seawater mixtures, resulted in saturation and deposition of sulfides, and of amorphous silica on existing sulfide surfaces as a thin layer [e.g., *Tivey et al.*, 1999]. Over time the precipitation of angular sulfide grains and coatings of silica decreased porosity, blocked flow pathways, and limited the permeability through the flange, similar to as described by *Zhu et al.* [2007] for samples from the Mothra Vent Field.

4.3. Lucky Strike Slabs

[26] The slab samples are composed of clasts of highly vesicular glass ± plagioclase of variable size, with amorphous silica rimming clasts and clay filling interstices (Table 2). Eleven thin sections were made from four slab samples: ALV2608-3-3 (2 sections), ALV2608-4-1, Pc 1 (Figures 5a and 5b; 3 sections), ALV2608-4-1, Pc 2 (3 sections), and JAS177-2-1 (3 sections) (Figure 3c), all cut through the cores such that layers were present in each section. Thin sections from five perpendicular-to-layering cores were examined to identify microstructural features that might explain the relatively steep ($\alpha \approx 8$) permeability/porosity trend for these cores. The thin section from the most permeable of the perpendicular-to-layering cores (ALV 2608-4-1, Pc 2 core 2) reveals moderately sorted, highly fragmented clasts (100 to 800 μm) of vesicular glass in each of its layers. A very thin

(5 μm) layer of amorphous silica and clay coats many of the glass clasts, and fills interstices; however, pore connectivity remains intact through each of the layers, delineated by variations in grain packing. The thin section from Core B3 of the same sample is very similar and contains layers of highly fragmented glass clasts, although within this section greater variability is apparent in grain packing and amounts of amorphous silica and clay. There are two layers visible within this section that can account for the somewhat lower measured permeability and porosity values: a layer of slightly smaller and more tightly packed clasts (Figure 5c) and a layer where pore space between grains has been almost entirely filled with amorphous silica and clay (Figure 5d). These restrictive features, more tightly packed clasts and more abundant amorphous silica and clay filling pore space, were not observed in the thin section from Core 2. The thin section from sample JAS177-2-1 core A2 is also composed of vesicular glass clasts, though clast size varies considerably through the different layers (30 to 900 μm), and abundant plagioclase clasts ($\sim$15%) varying from 20 μm to 2 mm in size are present. The clasts are widely spaced (with 50 to 200 μm between clast edges), but in several of the layers, clay and amorphous silica fill previous pore space, restricting connections between pores. Pore space in some layers is up to 70%, but in others much lower (10%). The lower permeability values can be attributed to the very low degree of pore connectivity in the low porosity layers. Thin sections from cores C3–1 and C3–2 of sample ALV2608-4-1, Pc 1 exhibit similar textures: a mixture of large and small glass clasts coated with amorphous silica. Much of the space between clasts has been infilled with clay that blocks connections between pores, isolating them. Microstructural observations are consistent with core C3–1 being least permeable, because it includes a layer with a large amount of clay and amorphous silica precipitation that has filled pore space and severely limited connections between pores.

[27] Thin sections from parallel-to-layering slab cores reinforce the observations from the previously described slab thin sections. The most, and least, permeable of these cores are from sample ALV2608-3-3. Thin sections from both cores B2 and C1 reveal poorly sorted glass clasts (and a few plagioclase clasts) coated with amorphous silica and minor clay. In the thin section from core B2, clasts are loosely packed, and the coating of amorphous silica decreases the width of spaces between pores, but seldom completely blocks connectivity
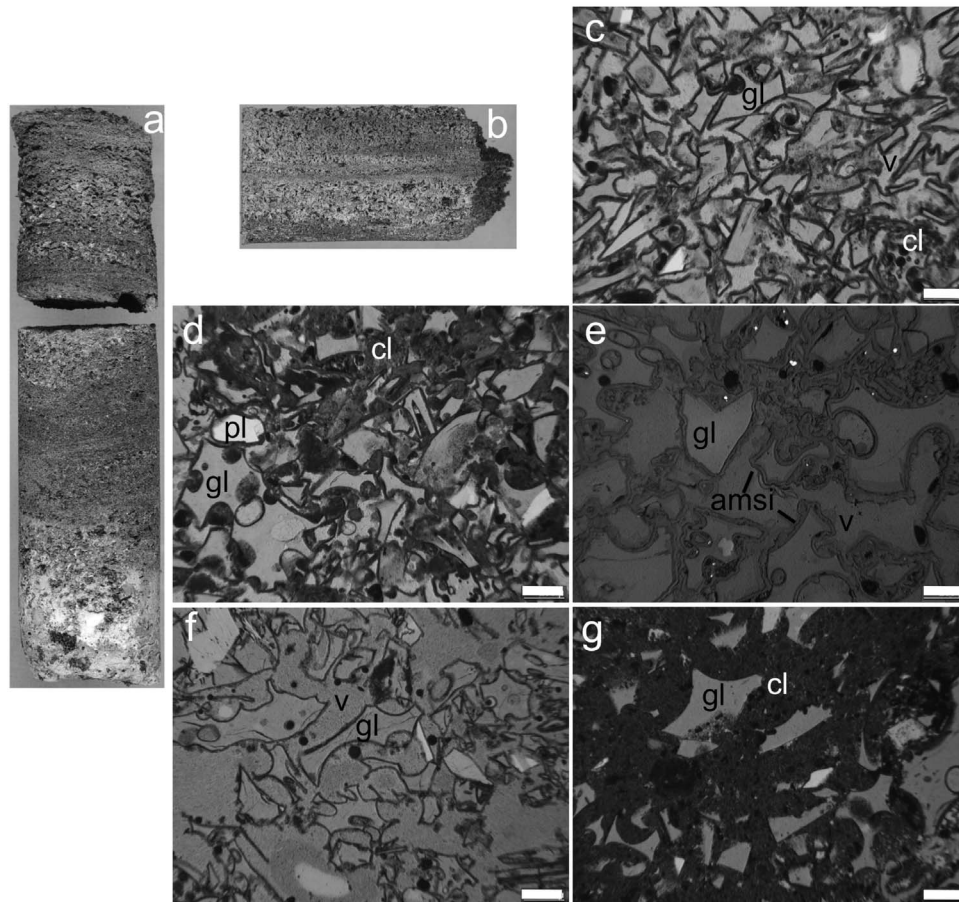
Figure 5. Slab cores (25.4 mm in diameter) and transmitted and reflected light photomicrographs from slab core thin sections. (a) Lucky Strike Vent Field slab core ALV2608-4-1 Pc 1 Core C3, taken perpendicular to layering, and (b) Core A2, taken parallel to layering. Transmitted light photomicrographs of the thin section from slab ALV2608-4-1 Pc 2 Core B3 showing (c) a layer of angular glass clasts (gl) that are more tightly packed than elsewhere in this core, as well as minor clay (cl) as a thin rind on clasts and partially filling interstices, and (d) a layer where pore space between glass and plagioclase (pl) clasts has been filled with amorphous silica and clay (cl); v is pore space, and scale bars are 200 μm. (e) Reflected light image of the thin section from slab ALV2608-3-3 Core B2 showing loosely packed glass clasts (gl) rimmed with amorphous silica. Note fine-grained pyrite (bright spots) co-precipitated with amorphous silica; v is pore space and scale bar is 200 μm. Transmitted light images from the thin section made from slab JAS177-2-1 Core B2 showing (f) a well connected, high porosity and thus likely high permeability layer of glass clasts (gl), versus (g) a layer of glass clasts (gl) with pore space that had been densely infilled with amorphous silica and clay (cl). The precipitation of amorphous silica and clay results in void space reduction, which generally leads to a loss of pore connectivity, thereby reducing permeability. Scale bars are 200 μm; v is pore space.

(Figure 5e). In the thin section from core C1, glass clasts are more densely packed than in core B1, and coatings of amorphous silica and clay are thicker, together resulting in less pore connectivity. However, grain packing is less dense, and pore connectivity greater, in the layer of core C1 nearest the top of the slab; this layer likely explains why the permeability of this core (made parallel to layering) has a high permeability despite a low porosity. Textures observed in the thin section from sample JAS177-2-1 cores B2 and B1 are very similar to those from core A2. As with core A2, there is considerable variability between the structure and packing, with both highly porous and well-connected layers (Figure 5f) alternating with a layer that has a large amount of amorphous silica coating clasts, and clay filling interstices (Figure 5g). Permeability of the cores oriented parallel-to-layering is likely controlled by the layer with the highest pore connectivity. The thin section from sample ALV2608-4-1, Pc 2 core A3 reveals both amorphous silica and clay precipitated throughout the
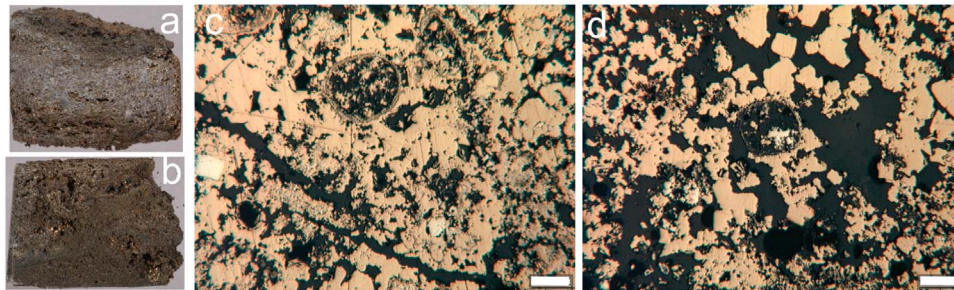
Figure 6. Crust cores (25.4 mm in diameter) and reflected light photomicrographs from crust core thin sections. (a) TAG active mound crust ALV2179-1-1 Core A1 taken perpendicular to layering and (b) Core B2, taken parallel to layering. (c) Reflected light image of the thin section from ALV2179-1-1 Core A1 showing an open crack that may have acted as a conduit, and (d) Reflected light image of the thin section from ALV2179-1-1 Core B2 showing high pore connectivity. Gold is chalcopyrite, yellow is pyrite/marcasite, dark gray/black is pore space, scale bars are 200 μm. Note ~250 μm diameter fossil tube worm casts in each image.

various layers, but pore space and pore connectivity are still both high, as in this sample's core 2. The core with the lowest permeability of the parallel-to-layering cores is ALV2608-4-1, Pc 1 core A1. The thin section from this core exhibits abundant amorphous silica and clay, and pore connectivity appears low through most of the layers compared with the other parallel-to-layering cores. Despite the abundance of amorphous silica and clay, flow through the core is controlled by the layers with highest connectivity. As a result, the parallel-to-layering permeability in this core is still relatively high.

[28] From a mineralogical and textural perspective, seafloor hydrothermal slabs can be classified as hydrothermally silicified volcaniclastic deposits. Layers, formed initially from settling of suspended fragments from the water column [*Eissen et al.*, 2003], are delineated by differences in clast size and initial packing density, and also by abundances of later precipitated amorphous silica and clay. The presence of amorphous silica and clay indicates that mixtures of silica-rich vent fluids and seawater percolated through the slabs, with cooling of the fluids resulting in saturation of amorphous silica [e.g., *Tivey et al.*, 1999] and clay, and precipitation along grain edges and in interstices. Observations indicate negligible precipitation of amorphous silica and clay in some layers, and abundant precipitation in others (e.g., Figures 5f and 5g).

[29] The slab samples are notable in that the perpendicular-to-layering cores plot at a slightly steeper trend than the other vent deposit sample groups (Figure 2), which may be due to the high angularity of the glass clasts, and the resultant large variability in pore shapes. Angular clasts create roughness along flow pathways that can

significantly impact the deposit's permeability. Differences in clast shape, which may not affect the total porosity significantly, can have a large effect on permeability. As a result, a steeper EPPR trend is produced.

4.4. TAG Crust

[30] Measurements were made on only one crust sample, ALV2179-1-1, and while it is not clear whether or not it is representative of other crust samples, results can be compared to those from other sulfide-rich layered samples, e.g., flanges. Thin sections were made from core A1 (a perpendicular-to-layering core) and core B2 (from a parallel-to-layering core) (Figures 3d, 6a, and 6b). The thin section from core A1 was cut along the radial direction of the cylindrical core through just one of the sample's layers. The layer is composed dominantly of fine- to medium-grained (20 to 500 μm) chalcopyrite and minor pyrite with pore space along grain edges. Pore connectivity in this layer is high, with throat sizes from 40 to 60 μm. Three open "cracks," which may act as conduits, are present, with widths of 40 to 80 μm (Figure 6c). Unfortunately, no information on pore connectivity in other layers of this sample is available. The thin section from core B2 was cut across the layering. Textures and mineral contents are similar to those in core A1. Layering was apparent only through changes in grain size (20 to 300 μm; Table 2). High pore connectivity is consistent through most of the layers (Figure 6d) and can explain the high permeability value.

[31] Because crust deposits on the TAG active mound are situated adjacent to high-temperature black smokers, fluids beneath the crust are likely

hot (around 300°C [*Tivey et al.*, 1995]). The crust sample is hypothesized to have developed much like sulfide flange deposits, with hot fluid percolating upwards from the base of the sample [*Tivey et al.*, 1995]. Textures are consistent with this interpretation. As with the flange samples, coarser-grained sulfide minerals are present at the bottom of the crust [*Tivey et al.*, 1995]. Packing of the grains is loose, providing space at grain boundaries to accommodate fluids moving up through the deposit. As the fluid travels upwards it cools, resulting in precipitation in pore spaces.

5. Discussion

[32] In this study, permeability and porosity measurements were conducted on flange, slab, and crust samples, each of which exhibit layering that parallels upper and lower surfaces of the deposits. Our data document that permeability values in the direction parallel to layering are considerably less variable and higher than permeability values in the direction perpendicular to layering. These differences in permeability suggest different flow behaviors controlled by layering, and have broad implications for the overall fluid flux accommodated by flange, slab, and crust seafloor deposits. At a given pressure gradient, such permeability structures imply that the dominant flow direction will likely be parallel-to-layering, within deposit layers of prominent highest permeability. Because permeability decreases little as porosity decreases (trend of $\alpha \approx 1$ or 2), this layering will continually facilitate the lateral flow of fluids through the deposits.

[33] The difference in magnitude as well as in variation of permeability values of cores taken parallel-to-layering versus perpendicular-to-layering in all samples can be quantified using an effective medium model. Because the total volume flux parallel to layering is equal to the sum of the volume flux through each layer (i.e., parallel flow connection), the effective permeability (k_{pal}) in this case is the sum of each layer's permeability (k_i) multiplied by the fraction of the total thickness (h_i/H), where h_i and H are the thickness of an individual layer and the total thickness of the sample, respectively [e.g., *Freeze and Cherry*, 1979]:

$$k_{pal} = \sum_{i=1}^{n} k_i \frac{h_i}{H} \qquad (2)$$

In contrast, the fluid flux perpendicular to layering must obey mass conservation while crossing several layers of varying permeabilities (i.e., serial flow connection). The effective permeability (k_{pep}) perpendicular-to-layering equals the total deposit thickness (H) divided by the sum of the ratios of layer thicknesses (h_i) to their respective permeabilities (k_i):

$$k_{pep} = H / \sum_{i=1}^{n} \frac{h_i}{k_i} \qquad (3)$$

From equations (2) and (3), it is easy to see that permeability of a layered vent deposit is generally anisotropic, with the parallel-to-layering effective permeability k_{pal} greater than the perpendicular-to-layering effective permeability k_{pep}.

[34] The parallel versus serial flow connections within the deposit cores are supported by microstructural observations from sample thin sections. Petrographic examination shows that the flange, slab, and crust deposits generally consist of layers with large contrasts in grain packing, void space, and pore connectivity (Figures 4–6). Low-permeability layers result from initial differences in grain packing, enhanced by subsequent precipitation in pore space. Low permeability layers restrict the overall flux perpendicular to layering thus exerting primary control on k_{pep}, whereas the flux parallel to layering is affected primarily by the highest permeability layer, which exerts primary control on k_{pal}. This explains why the permeability values in the parallel-to-layering cores are consistently higher than those in the perpendicular-to-layering cores and why the perpendicular-to-layering cores exhibit much greater permeability variation.

[35] This difference in parallel flow versus serial flow is best seen by comparing textures observed in thin sections from cores B1 and 2 of sample ALV2927–3 (Figures 4c and 4d). Both of these thin sections clearly show the same sequence of sample layering with some layers of relatively high pore connectivity (Figure 4f), and thus likely high permeability, and some with lower pore connectivity (Figure 4g) and thus likely lower permeability. Core B1, oriented parallel-to-layering, has a measured permeability over an order of magnitude greater than that of core 2, which was oriented perpendicular-to-layering.

[36] The microstructural observations provide explanations for the two EPPRs identified for these deposits. For the parallel-to-layering cores, with an EPPR with an exponent of $\alpha \approx 1$ to 2, the changes in the effective permeability of the samples are relatively small, even for large changes in porosity.

The thin sections taken from all of the cores show that the layers have undergone pore evolution through late-stage precipitation of amorphous silica and/or clays resulting in significant changes in porosity of the layers. An additional factor may be that precipitation of amorphous silica as a rind can initially result in smoother grain edges, affecting permeability.

[37] Microstructural observations support the presence of some layers with high permeability and others with low permeability, and the EPPR with exponent $\alpha \approx 1$ to 2 implies that decreases in porosity are accommodated within less porous layers, with the higher porosity of higher permeability layers maintained over time. The implication is that lower porosity layers fill with precipitates (e.g., amorphous silica and sulfide) more rapidly than higher porosity layers. In modeling quartz precipitation in hydrothermal upflow zones, *Martin and Lowell* [2000] carried out simulations that produced very similar results. They demonstrated that, in the case where linear kinetics of quartz precipitation was considered, narrower cracks would fill with silica more rapidly than wider cracks; while more fluid and thus more silica flowed through the wider cracks, the high flow rate resulted in the fluid traversing the crack before the silica could precipitate. In contrast, while less fluid and thus less silica traversed the narrower crack, the slower flow rate allowed the silica to precipitate.

[38] *Martin and Lowell* [2000] also discuss the significance of thermal gradients, noting that, for their study, the rate of quartz precipitation was controlled by the thermal gradient as well as by the rate of fluid flow through a crack. In the layered flange, slab, and crust samples, low permeability layers result in slow moving fluids that likely experience more cooling than fast moving fluids, leading to greater supersaturation, and conditions more favorable to precipitation within pore spaces. Higher flux rates in the higher permeability layers likely result in less cooling and less precipitation, and thus permeability reduction is less than in the lower permeability layers.

[39] For flow parallel to layers, as long as some high permeability layers remain, the overall permeability, or ability to transmit fluids, will remain high despite the overall sample's decrease in porosity. The overall permeability reduction in parallel-to-layering cores is gradual because in these cores, fluids pathways are in parallel connection (equation (2)). This is consistent with an EPPR with

an exponent of $\alpha \approx 1$–2 in parallel-to-layering cores observed in this study.

[40] Data from the perpendicular-to-layering cores reveal an EPPR with an exponent of $\alpha \approx 5$ to 8, and pore evolution processes that are significantly more effective in changing the overall permeability. Flow connection through these samples, perpendicular to layering, is serial (equation (3)). Changes in pore space of least permeable layers will restrict this serial flow and lower the effective permeability of the core.

[41] It is interesting to note that the three lowest permeability flange cores (Figure 2) plot close to a trend with an exponent of $\alpha \approx 8$, similar to data from the perpendicular-to-layering slab cores. This is also close to the trend observed in data from cores taken from inner portions of the three Mothra vent deposit samples studied by *Zhu et al.* [2007]. The trend with an exponent of $\alpha \approx 9$ in the Mothra samples was attributed to permeability evolution from deposition of more angular sulfide minerals versus the trend with an exponent of $\alpha \approx 3$ for outer portions of Mothra samples where permeability change resulted from porosity decrease from deposition of a coating of amorphous silica. In the layered flange/slab/crust samples, porosity decrease is occurring from both deposition of sulfide and amorphous silica, and, because the samples are layered, some scatter in the trend is expected. This scatter occurs because the measured porosity reflects the porosity of all layers, while the measured permeability is dominated by the permeability of the least permeable layer. Additionally, not all cores from a sample may include the same layers, so the dominant layer and its permeability can vary between cores. These effects of pore evolution processes on the sample layers and the effective permeability of the deposits are important for modeling their fluid fluxes.

6. Conclusions

[42] Measurements of permeability and porosity from seafloor flange, slab, and crust samples, can be used to identify permeability-porosity relationships, and document pronounced anisotropy. Our data demonstrate that fluids are able to more effectively pass horizontally through most permeable parallel layers in each sample rather than vertically across layers of different, including lower, permeability. The permeability and porosity data document pronounced anisotropy in flange, slab, and crust deposits, and microstructural observations

offer an explanation for this anisotropy: the presence of horizontal layers of high pore connectivity, and thus permeability, within all of these deposits. The documented anisotropy within these deposits has important implications for future efforts to model and constrain fluid fluxes from these vent deposits. Modeling work, such as that done on flanges by *Woods and Delaney* [1992], emphasizes the need for detailing factors that control the evolution of vent deposits. The growth of these deposits is dependent on the interplay between fluids and the vent deposits themselves. These interactions influence local flow rates, temperatures, and chemistry, and affect heat and mass flux through different parts of the vent deposits, and the availability of nutrients to organisms living in interiors and at exteriors of deposits. As such, having flow property data for vent samples is imperative for refining our understanding of seafloor hydrothermal processes.

Acknowledgments

References

Bernabé, Y., U. Mok, and B. Evans (2003), Permeability-porosity relationships in rocks subjected to various evolution processes, *Pure Appl. Geophys.*, *160*, 937–960, doi:10.1007/PL00012574.

Bohnenstiehl, D. R., R. P. Dziak, M. Tolstoy, C. G. Fox, and M. Fowler (2004), Temporal and spatial history of the 199–2000 Endeavour Segment seismic series, Juan de Fuca Ridge, *Geochem. Geophys. Geosyst.*, *5*, Q09003, doi:10.1029/2004GC000735.

Butterfield, D. A., R. E. McDuff, M. J. Mottl, M. D. Lilley, J. E. Lupton, and G. J. Massoth (1994), Gradients in the composition of hydrothermal fluids from the Endeavour segment vent field: Phase separation and brine loss, *J. Geophys. Res.*, *99*, 9561–9583, doi:10.1029/93JB03132.

Cooper, M. J., H. Elderfield, and A. Schultz (2000), Diffuse hydrothermal fluids from Lucky Strike hydrothermal vent field: Evidence for a shallow conductively heated system, *J. Geophys. Res.*, *105*(B8), 19,369–19,375, doi:10.1029/2000JB900138.

Delaney, J. R., V. Robigou, R. McDuff, and M. K. Tivey (1992), Geology of a vigorous hydrothermal system on the Endeavour Segment, Juan de Fuca Ridge, *J. Geophys. Res.*, *97*(B13), 19,663–19,682, doi:10.1029/92JB00174.

Eissen, J.-P., Y. Fouquet, D. Hardy, and H. Ondreas (2003), Recent MORB volcaniclastic explosive deposits from between 500 and 1750 m.b.s.l. on the axis of the mid-Atlantic Ridge, south of the Azores, in *Explosive Subaqueous Volcanism*, *Geophys. Monogr. Ser.*, vol. 140, edited by J. D. L. White, J. L. Smellie, and D. A. Clague, pp. 143–166, AGU, Washington, DC, doi:10.1029/140GM09.

Fisher, C. R., K. Takai, and N. Le Bris (2007), Hydrothermal vent ecosystems, *Oceanography*, *20*(1), 14–23, doi:10.5670/oceanog.2007.75.

Freeze, R. A., and J. A. Cherry (1979), *Groundwater*, Prentice Hall, Upper Saddle River, N. J.

Goldfarb, M. S., D. R. Converse, H. D. Holland, and J. M. Edmond (1983), The genesis of hot spring deposits on the East Pacific Rise, 21°N, in *Econ. Geol. Monogr.*, vol. 5, edited by H. Ohmoto and B. J. Skinner, pp. 184–197, Econ. Geol., Lancaster, Pa.

Hannington, M. D., and S. D. Scott (1988), Mineralogy and geochemistry of a hydrothermal silica-sulfide-sulfate spire in the caldera of Axial Seamount, Juan de Fuca Ridge, *Can. Mineral.*, *26*, 603–635.

Hannington, M. D., I. R. Jonasson, P. M. Herzig, and S. Petersen (1995), Physical and chemical processes of seafloor mineralization at mid-ocean ridges, in *Seafloor Hydrothermal Systems: Physical, Chemical, Biological, and Geological Interactions*, *Geophys. Monogr. Ser.*, vol. 91, edited by S. E. Humphris et al., pp. 115–157, AGU, Washington, D. C.

Haymon, R. M. (1983), Growth history of hydrothermal black smoker chimneys, *Nature*, *301*, 695–698, doi:10.1038/301695a0.

Haymon, R. M. (1996), The response of ridge crest hydrothermal systems to segmented, episodic magma supply, in *Tectonic, Magmatic, Hydrothermal, and Biological Segmentation of Mid-Ocean Ridges*, edited by C. J. MacLeod, P. Tyler, and C. L. Walker, *Geol. Soc. Spec. Publ.*, *118*, 157–168, doi:10.1144/GSL.SP.1996.118.01.09.

Haymon, R. M., and M. Kastner (1981), Hot spring deposits on the East Pacific Rise at 21°N: Preliminary description of mineralogy and genesis, *Earth Planet. Sci. Lett.*, *53*, 363–381, doi:10.1016/0012-821X(81)90041-8.

Kerr, R. C. (1997), Heat transfer and hydrothermal fluid flow at flanges on large seafloor sulphide structures, *Earth Planet. Sci. Lett.*, *152*, 93–99, doi:10.1016/S0012-821X(97)00137-4.

Koski, R. A., P. F. Lonsdale, W. C. Shanks, M. E. Berndt, and S. S. Howe (1985), Mineralogy and geochemistry of a sediment-hosted hydrothermal sulfide deposit from the Southern Trough of Guaymas Basin, Gulf of California, *J. Geophys. Res.*, *90*(B8), 6695–6707, doi:10.1029/JB090iB08p06695.

Koski, R. A., I. R. Jonasson, D. C. Kadko, V. K. Smith, and F. L. Wong (1994), Compositions, growth mechanisms, and temporal relations of hydrothermal sulfide-sulfate-silica chimneys at the northern Cleft segment, Juan de Fuca Ridge, *J. Geophys. Res.*, *99*, 4813–4832, doi:10.1029/93JB02871.

Kristall, B., D. S. Kelley, M. D. Hannington, and J. R. Delaney (2006), Growth history of an intermediate temperature, diffusely venting sulfide pinnacle from the Juan de Fuca Ridge: A petrological and geochemical study, *Geochem. Geophys. Geosyst.*, *7*, Q07001, doi:10.1029/2005GC001166.

Langmuir, C., et al. (1997), Hydrothermal vents near a mantle hot spot: The Lucky Strike vent field at 37°N on the Mid-Atlantic Ridge, *Earth Planet. Sci. Lett.*, *148*(1–2), 69–91, doi:10.1016/S0012-821X(97)00027-7.

Le Bris, N., M. Zbinden, and F. Gaill (2005), Processes controlling the physico-chemical microenvironments associated with Pompeii worms, *Deep Sea Res., Part I*, *52*, 1071–1083, doi:10.1016/j.dsr.2005.01.003.

Lilley, M. D., D. A. Butterfield, E. J. Olson, J. E. Lupton, S. A. Macko, and R. E. McDuff (1993), Anomalous CH_4 and NH_4^+

concentrations at an unsedimented mid-ocean ridge hydrothermal system, *Nature*, *364*, 45–47, doi:10.1038/364045a0.

Lilley, M. D., J. A. Lupton, D. A. Butterfield, and E. J. Olson (2003), Magmatic events can produce rapid changes in hydrothermal vent chemistry, *Nature*, *422*, 878–881, doi:10.1038/nature01569.

Lisitsyn, A. P., Y. A. Bogdanov, L. P. Zonenshayn, M. I. Kuz'min, and A. M. Podrazhanskiy (1989), Black smokers in the Gulf of California, *Int. Geol. Rev.*, *31*, 541–555, doi:10.1080/00206818909465907.

Lonsdale, P., and K. Becker (1985), Hydrothermal plumes, hot springs, and conductive heat-flow in the Southern Trough of Guaymas Basin, *Earth Planet. Sci. Lett.*, *73*(2–4), 211–225, doi:10.1016/0012-821X(85)90070-6.

Lowell, R. P., P. A. Rona, and R. P. Von Herzen (1995), Seafloor hydrothermal systems, *J. Geophys. Res.*, *100*(B1), 327–352, doi:10.1029/94JB02222.

Martin, J. T., and R. P. Lowell (2000), Precipitation of quartz during high-temperature, fracture-controlled hydrothermal upflow at ocean ridges: Equilibrium versus linear kinetics, *J. Geophys. Res.*, *105*(B1), 869–882, doi:10.1029/1999JB900342.

Peter, J. M., and S. D. Scott (1988), Mineralogy, composition, and fluid-inclusion microthermometry of seafloor hydrothermal deposits in the Southern Trough of Guaymas Basin, Gulf of California, *Can. Mineral.*, *26*, 567–587.

Robigou, V., J. R. Delaney, and D. S. Stakes (1993), Large massive sulfide deposits in a newly discovered active hydrothermal system, the High-Rise Field, Endeavour Segment, Juan de Fuca Ridge, *Geophys. Res. Lett.*, *20*, 1887–1890, doi:10.1029/93GL01399.

Rouxel, O., Y. Fouquet, and J. N. Ludden (2004), Subsurface processes at the Lucky Strike hydrothermal field, Mid-Atlantic Ridge: Evidence from sulfur, selenium, and iron isotopes, *Geochim. Cosmochim. Acta*, *68*(10), 2295–2311, doi:10.1016/j.gca.2003.11.029.

Schultz, A., J. R. Delaney, and R. E. McDuff (1992), On the partitioning of heat flux between diffuse and point source seafloor venting, *J. Geophys. Res.*, *97*, 12,299–12,314, doi:10.1029/92JB00889.

Thompson, G., M. J. Mottl, and P. A. Rona (1985), Morphology, mineralogy and chemistry of hydrothermal deposits from the TAG area, 26°N Mid-Atlantic ridge, *Chem. Geol.*, *49*, 243–257, doi:10.1016/0009-2541(85)90159-7.

Tivey, M. K. (1995), The influence of hydrothermal fluid composition and advection rates on black smoker chimney mineralogy: Insights from modeling transport and reaction, *Geochim. Cosmochim. Acta*, *59*, 1933–1949, doi:10.1016/0016-7037(95)00118-2.

Tivey, M. K., and J. R. Delaney (1986), Growth of large sulfide structures on the Endeavour Segment of the Juan de Fuca Ridge, *Earth Planet. Sci. Lett.*, *77*, 303–317, doi:10.1016/0012-821X(86)90142-1.

Tivey, M. K., and R. E. McDuff (1990), Mineral precipitation in the walls of black smoker chimneys: A quantitative model of transport and chemical reaction, *J. Geophys. Res.*, *95*(B8), 12,617–12,637, doi:10.1029/JB095iB08p12617.

Tivey, M. K., S. E. Humphris, G. Thompson, M. D. Hannington, and P. A. Rona (1995), Deducing patterns of fluid flow and mixing within the TAG active hydrothermal mound using mineralogical and geochemical data, *J. Geophys. Res.*, *100*(B7), 12,527–12,555, doi:10.1029/95JB00610.

Tivey, M. K., D. S. Stakes, T. L. Cook, M. D. Hannington, and S. Petersen (1999), A model for growth of steep-sided vent structures on the Endeavour Segment of the Juan de Fuca Ridge: Results of a petrologic and geochemical study, *J. Geophys. Res.*, *104*(B10), 22,859–22,883, doi:10.1029/1999JB900107.

Turcotte, D. L., and G. Schubert (1982), *Geodynamics: Applications of Continuum Physics to Geological Problems*, Cambridge Univ. Press, New York.

Veirs, S. R., R. E. McDuff, and F. R. Stahr (2006), Magnitude and variance of near-bottom horizontal heat flux at the Main Endeavour hydrothermal vent field, *Geochem. Geophys. Geosyst.*, *7*, Q02004, doi: 10.1029/2005GC000952.

Von Damm, K. L., J. M. Edmond, C. I. Measures, and B. Grant (1985), Chemistry of submarine hydrothermal solutions at Guaymas Basin, Gulf of California, *Geochim. Cosmochim. Acta*, *49*, 2221–2237, doi:10.1016/0016-7037(85)90223-6.

Walsh, J. B. (1965), The effect of cracks on the compressibility of rock, *J. Geophys. Res.*, *70*(2), 381–389, doi:10.1029/JZ070i002p00381.

Woods, A. W., and J. R. Delaney (1992), The heat and fluid transfer associated with the flanges on hydrothermal venting structures, *Earth Planet. Sci. Lett.*, *112*, 117–129, doi:10.1016/0012-821X(92)90011-J.

Zhu, W., B. Evans, and Y. Bernabé (1999), Densification and permeability reduction in hot-pressed calcite: A kinetic model, *J. Geophys. Res.*, *104*, 25,501–25,511, doi:10.1029/1999JB900230.

Zhu, W., M. K. Tivey, H. Gittings, and P. R. Craddock (2007), Permeability-porosity relationships in seafloor vent deposits: Dependence on pore evolution processes, *J. Geophys. Res.*, *112*, B05208, doi:10.1029/2006JB004716.